BIOMIMETICS

Soft biohybrid morphing wings with feathers underactuated by wrist and finger motion

Eric Chang*, Laura Y. Matloff*, Amanda K. Stowers*, David Lentink†

Since the Wright Flyer, engineers have strived to develop flying machines with morphing wings that can control flight as deftly as birds. Birds morph their wing planform parameters simultaneously—including sweep, span, and area—in a way that has proven to be particularly challenging to embody robotically. Previous solutions have primarily centered around the classical aerospace paradigm of controlling every degree of freedom to ensure predictable performance, but underperform compared with birds. To understand how birds accomplish wing morphing, we measured the kinematics of wing flexion and extension in common pigeons, *Columba livia*. The skeletal and feather kinematics show that the 20 primary and 20 secondary feathers are coordinated via approximately linear transfer functions controlled by wrist and finger motion. To replicate this control principle in a robot, we developed a biohybrid morphing wing with real feathers to understand the underlying design principles. The outcome, PigeonBot, embodies 42 degrees of freedom that control the position of 40 elastically connected feathers via four servo-actuated wrist and finger joints. Our flight tests demonstrate that the soft feathered wings morph rapidly and robustly under aerodynamic loading. They not only enable wing morphing but also make robot interactions safer, the wing more robust to crashing, and the wing reparable via "preening." In flight tests, we found that both asymmetric wrist and finger motion can initiate turn maneuvers—evidence that birds may use their fingers to steer in flight.

INTRODUCTION

Current aircraft use wing ailerons to initiate turn maneuvers and wing flaps and slats to increase lift and drag during takeoff and landing (*1*, *2*). Whereas moving these discrete wing elements has proven to be a successful strategy for efficient and agile flight, an aircraft's ability to change the shape of its wing is less sophisticated compared with how bats and birds morph their wings continuously in flight (*3*, *4*). This extreme form of wing morphing improves the flight efficiency and agility of bats and birds. For example, wing morphing enables the common swift to glide 60% further and 100% longer—in addition to enabling much faster and tighter turns—as compared with its glide performance with a fixed wing shape (*5*). Whereas these birds and other flying animals can continue flying with substantial wing damage (*4*), including feather molt (*6*), current aircraft need to pass rigorous preflight inspections before they are allowed to take off. Consequently, current engineering designs are less robust, efficient, maneuverable, and versatile when compared at the same scale as animals (*4*). Inspired by nature, engineers have developed new morphing wings that control wing planform sweep, span, chord, out-of-plane twist, and dihedral angle, as well as airfoil camber and thickness (*7*). The design of current aircraft control surfaces as well as these new morphing modalities requires special attention to balancing their mass and inertia, as well as actuating each degree of freedom in a closed-loop fashion (*1*, *2*, *7*, *8*). As a result, the integral design of modern morphing wings gets more complex for every additional degree of freedom added. For this reason, wing morphing is usually simplified to morphing either the airfoil or a subset of wing planform parameters (*7*).

The control of novel morphing degrees of freedom can be reframed as a bioinspired robotics challenge, because flying vertebrates use their limbs to morph their wings under musculoskeletal control (*4*), akin to a robot arm under closed-loop control (*9*). For example, bat wing shape is controlled via an articulated skeleton with at least 34 degrees of freedom, of which at least 25 are controlled (*10*). Furthermore, the sophisticated soft membrane skin of bats is actively tensioned by embedded muscles to streamline the airfoil (*11*). This has inspired roboticists to design morphing wings with highly deformable (*10*) and stretchable (*12*) membranes under closed-loop control of an articulated mechanical skeleton. Recently, one of these robots successfully demonstrated bat-inspired wing morphing in flight (*12*). Despite their sophisticated membrane tensioning, even bat wings are prone to membrane wrinkling when flexing the wing too much. Pennycuick (*13*) found that whereas bat skin will start to wrinkle and become aerodynamically inefficient during wing flexion, feathered bird wings remain streamlined. Birds accomplish this feat by overlapping their primary and secondary feathers (Fig. 1A) during wing flexion, embodying more articulated degrees of freedom beyond skeletal (*14*) via their numerous feathers, in particular, their flight feathers. These remiges are embedded in the postpatagium (Fig. 1A), which consists of smooth muscular tissue and ligament for which the function is not fully understood (*15*, *16*). Unlike skeletal muscle, smooth muscles have a limited control bandwidth, much slower than the avian wingbeat, to more economically maintain muscle tone (*17*). Therefore, it is unclear how feather motion and skeletal motion are coupled dynamically. Consequently, we do not fully understand how birds morph their wing parameters rapidly to unusual degrees (*5*, *16*).

Creating bird-inspired robots with feathered morphing wings has been an active area of research for almost two decades (*4*). RoboSwift was among the first flying aerial robots with feathered morphing wings; the eight carbon fiber feathers were engineered by eye to match the planform of a morphing swift wing (*5*, *18*). A prototype of RoboSwift demonstrated asymmetric wing morphing in the laboratory, whereas in flight it demonstrated symmetric wing morphing.

Department of Mechanical Engineering, Stanford University, Stanford, CA, USA.
*These authors contributed equally to robot development.
†Corresponding author. Email: dlentink@stanford.edu

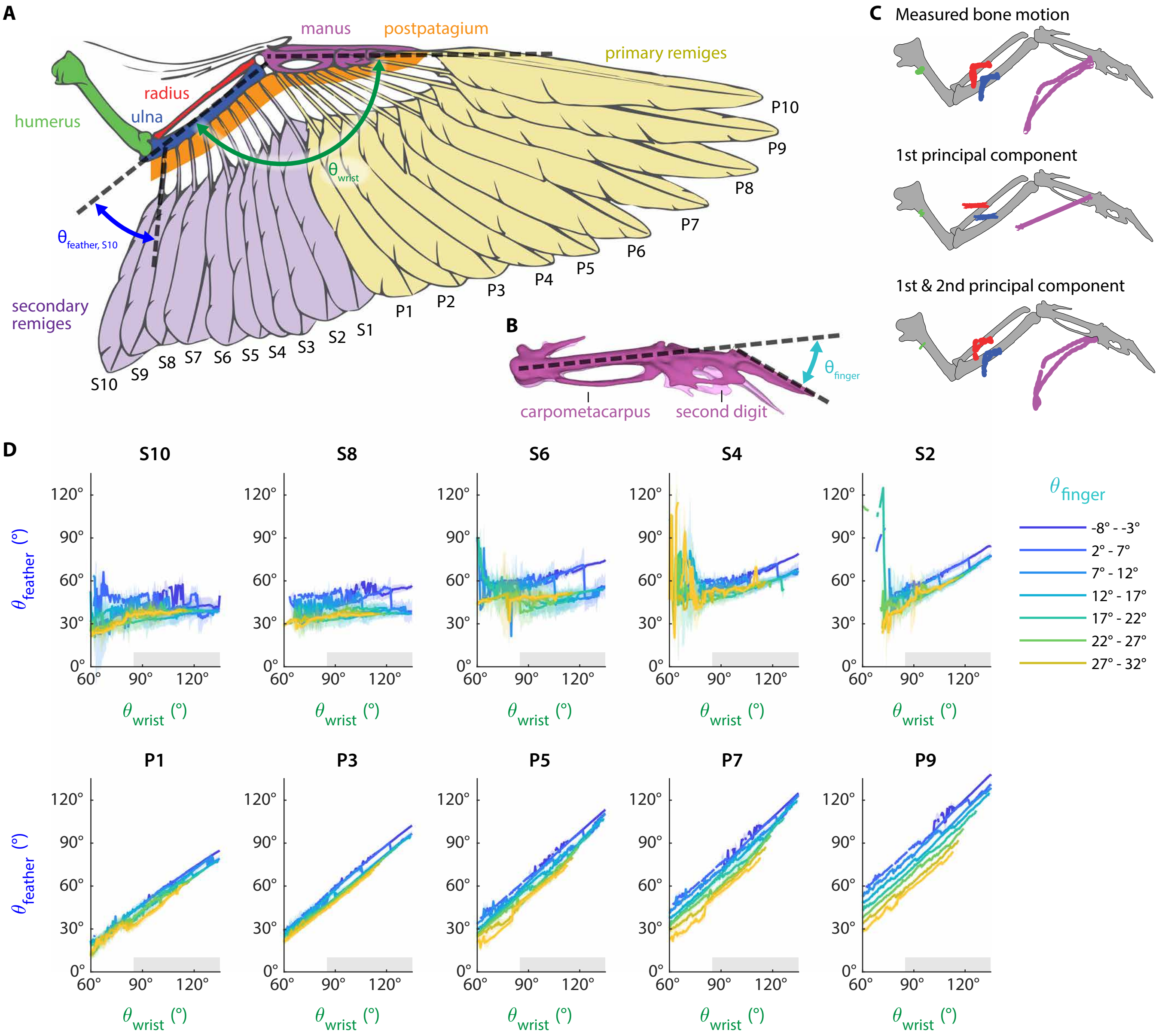

Fig. 1. Wrist and finger angles are the primary driver of avian wing morphing. (**A**) The four major bones in a pigeon (*C. livia*) wing are the humerus, radius, ulna, and manus. The 20 flight feathers (remiges) comprise 10 primary and 10 secondary feathers, which insert into the manus and ulna bones, respectively, and are embedded in the postpatagium tissue. We define the feather angle, $\theta_{feather}$, as the angle from the ulna to each feather. The ulna and carpometacarpus meet at the wrist with angle θ_{wrist}. The postpatagium consists of elastic ligament and smooth muscles that connect around the proximal base of each feather. Pigeon wing drawing adapted from Proctor and Lynch (*44*). (**B**) Within the manus, the carpometacarpus and distal phalanx of the second digit form the finger angle, θ_{finger}. An additional pose showing the range of motion of the second digit is shown for illustration purposes in light pink based on earlier work (*14*). (**C**) The first principal component represents more than 75% of the 3D measured skeletal motion during animated wing flexion and extension [for measurement details, see (*14*)]. Adding the second principal component captures 97% of the 3D measured skeletal motion (radius, red; ulna, blue; manus, purple trace). (**D**) Pigeon wing feather angles correlate linearly with wrist angles and finger angles. Distal primary feather angles (wing tip) are more sensitive to wrist and finger angles than proximal secondary feather angles (wing root). Gray horizontal bars on the horizontal axis indicate the range over which PigeonBot's biohybrid wing morphs. Solid lines indicate average angles and shaded regions indicate the standard deviation.

A follow-up robot, iMorph, featured 14 feather-inspired wing segments in conjunction with inextensible nylon cord to prevent overextension during symmetric wing morphing (*19*). Recently, an aerial robot demonstrated asymmetric morphing in flight using two morphing hand wings with 18 feathers made out of a carbon fiber shaft with a glass fiber frame and airtight fabric covering, each with the shape of four-sided polygons (*20*). However, all these robots have stiff engineered feather-like panels and controlled the planform rudimentarily as compared with birds. Progress in fluid planform morphing under robotic control is impeded by a lacking mechanistic understanding of how birds morph their soft feathered wings via skeletal-feather motion coupling. Resolving these coupling relationships will offer new bioinspiration for designing multifunctional morphing wings. Furthermore, harnessing these principles to recreate a morphing robot wing with real bird feathers introduces the opportunity to study how birds control their flight by repositioning their feathers in a fashion that cannot be accomplished in vivo.

RESULTS

To formulate the robotic design principles for soft feathered morphing wings, we measured the kinematics of feathers as a function of both wrist and finger angle in animated pigeon cadavers using high-resolution motion capture (Materials and Methods). From these measurements, we derived the most parsimonious principles that explain how a bird articulates its flight feathers during wing morphing using the left and right wrist and finger joints as four independently controlled degrees of freedom. Next, we used these design principles to develop a biohybrid morphing wing with 40 underactuated pigeon feathers, which are soft, robust, and light compared with previous robot feathered wings made from carbon and glass fiber. To test the effectiveness of our underactuated soft biohybrid morphing wing, we flexed and extended the wing dynamically in a wind tunnel and determined the robotic feather transfer functions under aerodynamic loading. Last, we demonstrate how asymmetric wing planform control via wrist and finger motion initiates turning flight in our new soft biohybrid aerial robot: PigeonBot.

Table 1. The first principal component explains at least 75% of the variation in wing shape during gliding in pigeons. Together, the first two principal components (PCs) represent at least 97% of the variation. This implies that a two–degree of freedom mechanism replicates almost all measured wing motion and that a single–degree of freedom mechanism represents the majority of the motion.

Individual	PC1	PC2	PC3	PC4	PC5
Pigeon 1	74.5%	22.5%	1.64%	0.48%	0.38%
Pigeon 2	92.2%	4.94%	1.62%	0.55%	0.34%
Pigeon 3	86.4%	9.85%	2.37%	0.63%	0.23%

Bird skeletal-feather coupling

To understand how flight feather motion is coordinated in bird wings as a function of wrist and finger motion, we performed a motion capture study of pigeons (*Columba livia*; $N = 3$ individuals). We cyclically animated the wing following the path of least resistance during which the wing morphed from fully extended, intermediate,

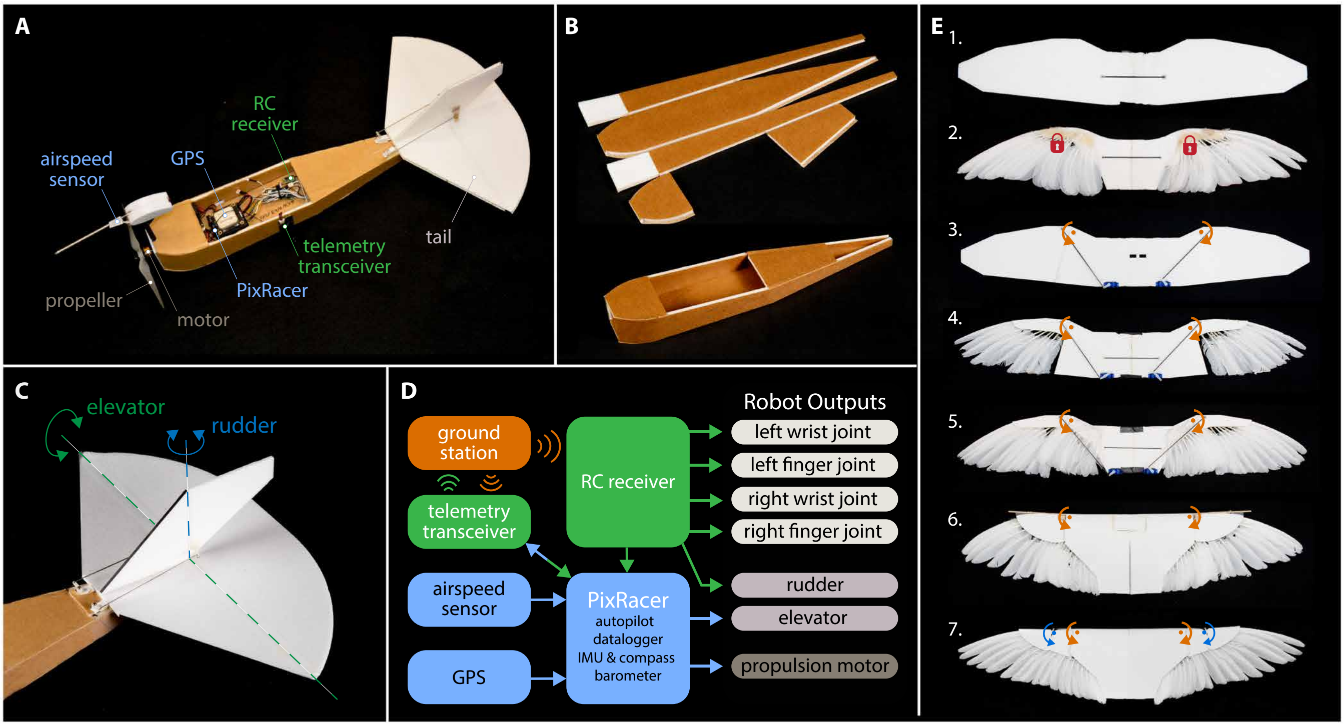

Fig. 2. PigeonBot: A soft biohybrid aerial robot consists of a propeller-driven instrumented body with an underactuated feathered morphing wing. (**A**) PigeonBot's body includes a propeller-driven electric propulsion system, sensors (GPS, pitot tube, barometers, and three-axis accelerometers, gyroscopes, and magnetometers), radios, an autopilot with data logging (PixRacer R14), and a tail. (**B**) The body is constructed from a single piece of laser-cut foamboard that is folded and glued together. (**C**) The foam tail has a conventional configuration with an elevator for longitudinal control and a rudder for lateral control. (**D**) The system block diagram shows how each actuator is controlled. For our wing morphing flight experiments, the ground station commands a wing pose, neutral static rudder, and constant propulsion throttle, whereas the elevator is under closed-loop control to sustain the robot's pitch. (**E**) The morphing wing was designed through iterative steps that were all successfully flight-tested. The successive steps were as follows: static pigeon wing planforms made out of foamboard (1); a fully extended planform with pigeon feathers glued to a foamboard skeleton (2); a simple one–degree of freedom foamboard "swing wing" with actuated wrists (3); primary feathers glued on a foamboard leading edge to form a feathered hand wing (4); primary and secondary feathers glued to an articulated one–degree of freedom foamboard skeleton forming the hand and arm (5); elastic bands added between each feather so that the feathers moved relative to each other rather than as discrete hand and arm panels (6). Last, we added an additional skeletal finger joint (7) to improve the range of planforms achieved by the biohybrid morphing wing (Fig. 4C).

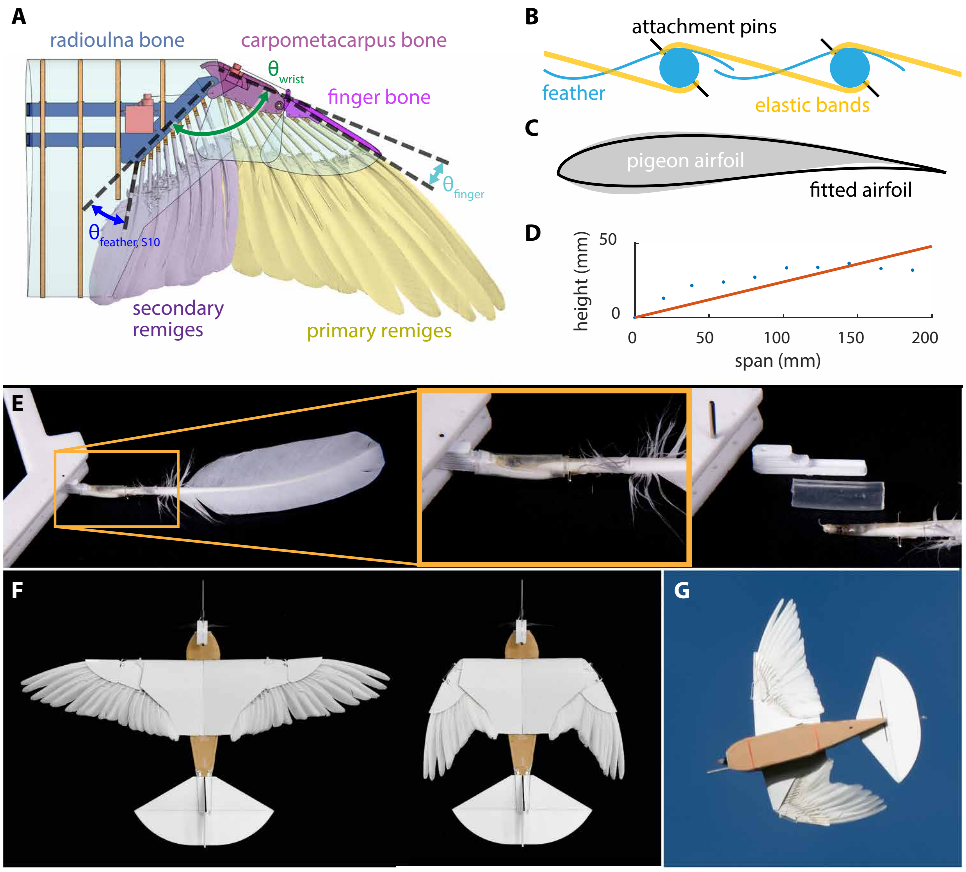

Fig. 3. Biological principles inform detailed biohybrid morphing wing design. (**A**) We integrated all 10 primary and 10 secondary remiges in the biohybrid wing. Each feather is mounted via pin joints to a simplified artificial skeleton consisting of a static fused "radioulna" bone and directly actuated carpometacarpus and finger bones. By directly actuating θ_{wrist} and θ_{finger} with servomotors, we underactuate all the feather angles ($\theta_{\mathrm{feathers}}$). Cardstock (shown in light blue) covered portions of the wing normally covered by covert feathers in a bird wing. (**B**) Independent rubber bands link each feather pair to recreate the feather motion that we recorded in bird cadavers. (**C**) We fitted in vivo gliding pigeon wing data (*23*) to a database of existing low–Reynolds number airfoils (https://m-selig.ae.illinois.edu) to determine the most representative shape for the root section of the biohybrid wing. (**D**) Similarly, we fitted these data to a linear model to determine the dihedral angle for our biohybrid wing. (**E**) We attached all 20 remiges to mechanical pin joints via custom 3D-printed feather interfaces that mount the feather with adhesive heat shrink. We adjusted the orientation of the feather after assembly by heating the thermoplastic feather interfaces and posing the feather in the desired pose. (**F**) The completed biohybrid wing enables large wing shape changes harnessing the passive softness of overlapping pigeon feathers, which we flight-tested outdoors (**G**).

and tucked wing planforms recorded for a gliding pigeon (*21*). We first animated the wing via the manus ($n = 12$ wing flexion and extension cycles) and then via the root of the distal feather P10 ($n = 12$ wing flexion and extension cycles), which is rigidly connected to the finger (Fig. 1; see Materials and Methods for details). In a previous study in which we only animated the root of P10, we reported the wing skeletal kinematics of the major wing bones; the coupling between the ulna, radius, and manus (hand) with respect to the humerus (Fig. 1A); and how the distal phalanx of the second digit (the finger of the wing; Fig. 1B) refines wingtip motion by rotating up to 30° independently (*14*). Here, we present further results based on a principal components analysis of the skeletal kinematics (Fig. 1C) across three pigeons (Table 1), which demonstrates that the first principal component represents at least 75% of the measured skeletal kinematics. Combined, the first and second principal components represent at least 97% of the skeletal kinematics underpinning wing flexion and extension, indicating that the skeletal mechanism is explained by one or two principal components. However, the principal components represent a 24-dimensional (24D) parameter space based on the six degrees of freedom of the four bones; therefore, we need to consider how they correlate to measurable degrees of freedom that are directly actuatable in a robot. We found that the first principal component correlates 97% with the wrist angle, which connects the arm (secondary feathers) and hand (primary feathers) wing. On the basis of these findings, we simplified our skeletal-feather coupling analysis by focusing on the wrist and finger angle as robotic input parameters. The measured relationships between the feather angle, $\theta_{\mathrm{feather}}$, defined as the angle of each of the 20 remiges with respect to the ulna, and the wrist angle, θ_{wrist}, defined as the angle between the ulna and carpometacarpus, are approximately linear (Fig. 1D). The relationship is modified by the finger angle, θ_{finger}, the angle between the carpometacarpus and second digit, which offsets the relationship between wrist and feather angle (Fig. 1D). The coupling relationships are better defined for the primary feathers in the hand wing, because the measurements of the secondary feathers in the arm wing are noisier due to tracking errors caused by the feather overlap obscuring markers during extreme flexion. Regardless, the overall coupling relationships are close to linear. The linearity suggests that the postpatagium (Fig. 1A) functions as a tunable linearly elastic band that passively couples wrist and finger motion to feather motion, and therefore, the feathers could simply be underactuated during morphing.

PigeonBot test platform

We developed a biohybrid aerial robot platform, PigeonBot, to rigorously test whether the approximately linear wrist-finger-feather coupling relationships can be accomplished passively with tuned rubber bands and to determine the role of the finger in flight control. The robot control system comprises an autopilot (PixRacer R14 with integrated inertial measurement unit), a GPS, a pitot tube, radio transceivers, servo actuators that control the conventional tail, and a motor-driven propeller for propulsion (Fig. 2A). The fuselage, which carries this control system, is cut out of a single piece of foamboard that is folded into its 3D shape and glued together in subsequent steps (Fig. 2B). The conventional tail is made

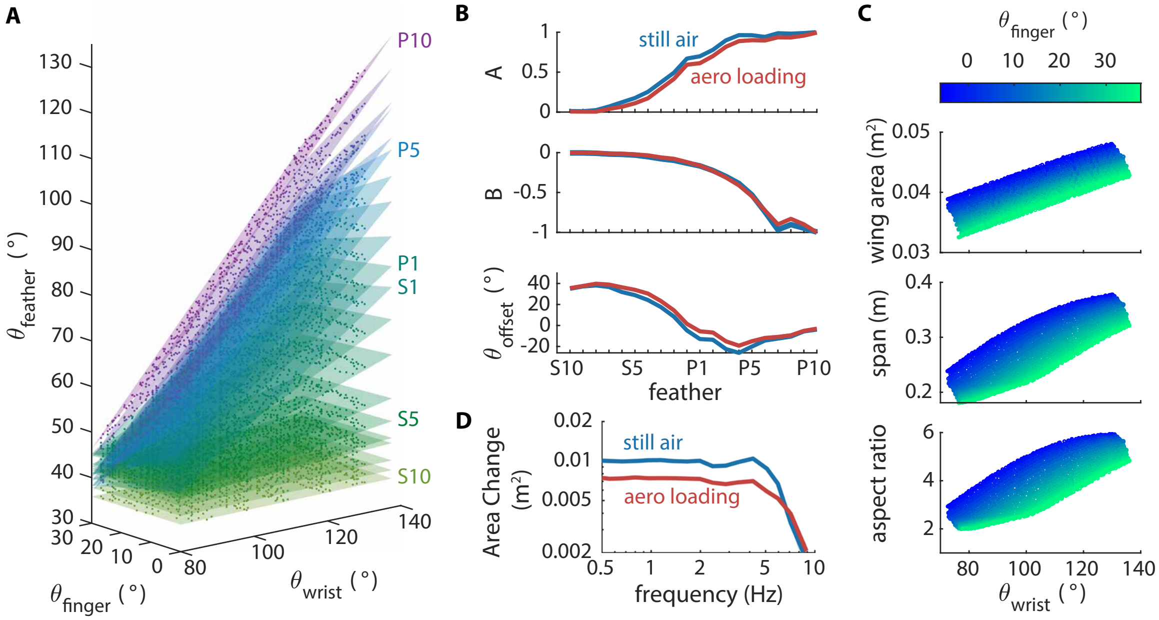

Fig. 4. Wrist and finger angles dynamically drive the motion of 20 feathers under aerodynamical loading. (**A**) We measured the biohybrid morphing wing kinematics in a wind tunnel at the same mean speed and angle of attack measured in outdoor flights (11.7 m s^{-1} and 4.4°; Materials and Methods). Under these quasi-static conditions in which the wing flexes and extends θ_{wrist} at 0.4 Hz for 42 cycles, while cycling θ_{finger} at 0.01 Hz, θ_{feather} is approximately a linear function of θ_{wrist} and θ_{finger} (RMSE: 0.87°). (**B**) Fitted coefficients of the corroborated linear feather angle model show how distal feathers are more sensitive to θ_{wrist} and θ_{finger}, *B* than proximal feathers. (**C**) The combinations of wrist and finger angle afford a wide configuration space of wing area, span, and aspect ratio under aerodynamic loading. (**D**) The response of the biohybrid wing to full flexion-extension commands at varying frequencies demonstrates a system bandwidth up to 5 Hz due to servo limitations.

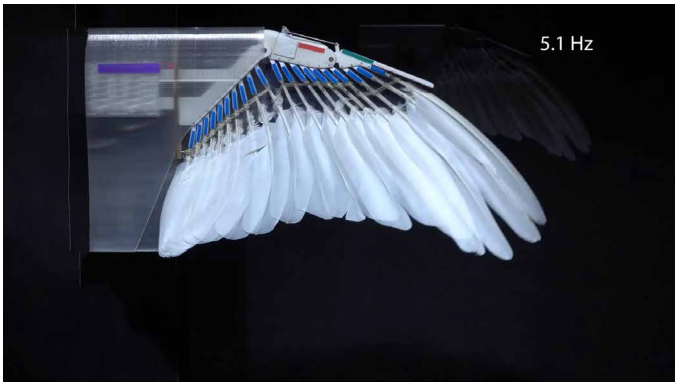

Movie 1. Morphing wing response to increasing flexion/extension cycling frequency under aerodynamic loading. A subset of the cycling frequencies tested (0.4, 1.0, 2.0, 5.1, and 8.9 Hz) shows that the PigeonBot wing responds well to control inputs up to ~5 Hz.

out of foam with carbon fiber strips along the leading edge, and the elevator and rudder hinges consist of tape. To ensure PigeonBot flies sufficiently stably across all morphed states with minimal autopilot input for the elevator, we optimized the tail volume through preliminary flight tests with fixed foamboard wings. The wings replicated the fully extended, intermediate, and tucked wing planforms reported for gliding pigeons (details in the Supplementary Materials) (*21*).

Soft underactuated biohybrid morphing wing

Through systematic bioinspired prototyping, we designed a highly repeatable soft biohybrid morphing wing, with real pigeon flight feathers that are underactuated through a biomimetic elastic ligament under skeletal control. Real feathers offer many advantages over our earlier carbon fiber artificial feather designs (*18*), because they are softer, lighter, more robust, and easier to get back into shape after a crash by simply preening ruffled feathers between one's fingers. We flight-tested all prototypes successfully before embarking on the next level of complexity. Our first biohybrid wing prototype consisted of the pigeon flight feathers simply glued in their fully extended position to a foamboard skeleton (Fig. 2E). Integrating the pigeon feathers in our first biohybrid wing prototypes posed unexpected engineering challenges. Whereas traditional manufacturing produces precise and repeatable parts, we observed qualitatively that biological variation between pigeon individuals is too large to exchange a particular flight feather between different individuals without compromising the wing planform. Accordingly, we found that manufacturing of the biohybrid morphing wing is accurate and repeatable, provided that feathers from a single individual are used. The primary and secondary flight feathers need to be integrated in the exact same order (Fig. 1A), with as few replacement feathers from other individuals as possible. Within these constraints, we were able to reproduce our wing design going from one prototype to the next (Fig. 2E). We thus only substituted feathers from other similarly sized individuals for missing or damaged feathers when needed (table S1). In our effort to maximize morphing repeatability, we found based on subsequent prototypes (details in the Supplementary Materials) that finger motion is needed in addition to wrist motion to faithfully reproduce both fully extended and tucked pigeon wing planforms (Fig. 3A and fig. S2), that individual rubber bands are needed between each feather pair to underactuate feather motion reliably (Fig. 3B, fig. S2, and tables S2 and S3), and that the feather holders need to be adjustable after fabrication to form a closed feathered surface (Fig. 3E).

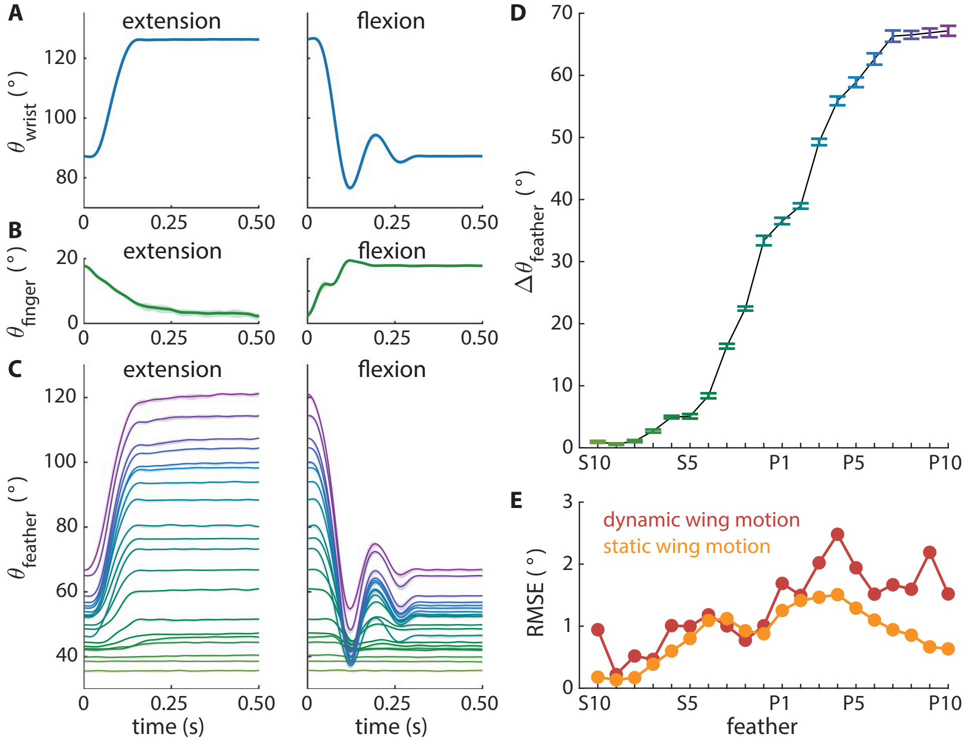

Fig. 5. The quasi-static linear transfer functions, between wrist and finger input to feather angle output, approximate the measured dynamic response under aerodynamic loading well. (**A** and **B**) The measured wrist, θ_{wrist}, and finger, θ_{finger}, angle kinematics resulting from step commanding the wrist and finger servos to extend and flex, respectively, the wing at maximal speed. The deviation from a step response in the wrist and finger kinematics is due to the biohybrid morphing wing's (including servo motors) elastic, damping, and inertia properties under aerodynamic loading. The wrist and finger extension response is characteristic of an overdamped system, whereas the flexion response is characteristic of an underdamped system. (**C**) Visual inspection of the measured dynamic response of each flight feather to combined wrist (A) and finger (B) actuation suggests that the input and output kinematics are directly correlated. In (A) to (C), solid lines indicate average angles and shaded regions indicate the standard deviation. (**D**) The range of feather motion over a full extension and flexion cycle ($\Delta\theta_{\text{feather}}$) is largest for distal feathers, with $\Delta\theta_{\text{P10}} \approx 70°$. The small standard deviation (error bars) in feather motion range shows the high repeatability of the feather underactuation mechanism. (**E**) The quasi-static linear feather-angle transfer function (Fig. 4A) reproduces the measured feather kinematics of the slow morphing wing well (mean RMSE: 0.87°, morphing θ_{wrist} at 0.4 Hz for 42 flexion and extension cycles; see Fig. 4 for details). The same quasi-static transfer function predicts the measured feather kinematics similarly well (mean RMSE: 1.31°) when the biohybrid wing morphs dynamically at maximal speed [(A) to (C); 10 flexion and extension cycles]. The *y* axis of the feather angle error (E) was magnified 10× compared with the plot of feather motion range (D) to aid visual comparison.

We integrated these key prototype findings in our final soft underactuated biohybrid morphing wing design (Figs. 2E and 7). The resulting 3D printed design features an independently servo-actuated wrist and finger joint (Fig. 3A) with simplified smaller feather interfaces that can be deformed with a heat gun to tune each feather's orientation after mounting (Fig. 3E). The tuned rubber ligament design comprises a series of individual dental rubber bands (Fig. 3B and fig. S1) that are carefully selected for appropriate stiffness (tables S2 and S3). The rubber bands apply a torsional stiffness of about 0.04 Nm/rad, which is within the stiffness range of 0.0005 to 0.05 Nm/rad estimated for the postpatagium they mimic (Supplementary Materials). The bands were tuned so that the biohybrid wing's passive feather positions match two measured morphing wing states: extended and tucked (fig. S2). The rubber band attachment points on each feather are oriented such that the tensioned bands passively press the feather vanes together (Fig. 3B), which were inspired by how smooth muscles wrap around the feather follicles (*22*). The root airfoil design of the skeleton is based on earlier measurements of in vivo wing shape in gliding pigeons (*23*), to which we fitted comparable low–Reynolds number airfoils (Fig. 3C). To determine the dihedral angle, we linearly fit a line to the wing section height distribution from the same in vivo gliding pigeon data (Fig. 3D). Last, we covered the two–degree of freedom robot arm and the exposed feather shafts with cardstock to improve the streamline of the wing and minimize aerodynamic leakage. This simplification, in which we roughly approximate the function of the covert and other specialized feathers that streamline the wing, was required to bound the manufacturing complexity of the biohybrid wing while capturing the measured features (for design details, see Materials and Methods).

Our biohybrid morphing wing is an underactuated robotic system according to Tedrake's mathematical definition (*24*): The kinematic configuration vector of the morphing wing half is

$$\mathbf{q} = [\theta_{\text{wrist}}, \theta_{\text{finger+P10}}, \theta_{\text{P9}}, \theta_{\text{P8}}, \cdots, \theta_{\text{S9}}, \theta_{\text{S10}}]^T \tag{1}$$

in which θ is the angle of the wrist, finger, primary (P1 to P9), and secondary (S1 to S10) feathers, and P10 is fused to the finger. The servo-based control vector of the wing half is

$$\mathbf{u} = [\theta_{\text{wrist}}, \theta_{\text{finger+P10}}] \tag{2}$$

which drives the dynamic response of the morphing wing half

$$\ddot{\mathbf{q}} = \mathbf{f}_1(\mathbf{q}, \dot{\mathbf{q}}, t) + \mathbf{f}_2(\mathbf{q}, \dot{\mathbf{q}}, t)\,\mathbf{u} \tag{3}$$

Following Tedrake (*24*), we find that the rank of the control term is an order of magnitude smaller than the rank of the configuration vector

$$\text{rank}\,[\,\mathbf{f}_2(\mathbf{q}, \dot{\mathbf{q}}, t)\,] = 2 < \text{rank}\,[\,\mathbf{q}\,] = 21 \tag{4}$$

Consequently, the robot system is underactuated, because the control vector **u** cannot command arbitrary instantaneous accelerations in all of **q**'s degrees of freedom. The resulting biohybrid PigeonBot morphs its soft feathered wing fluidly based on elastic underactuation of 40 flight feathers, of which only the left and right P10 are under closed-loop control by two wrist and two finger joints in the wing (Fig. 3F).

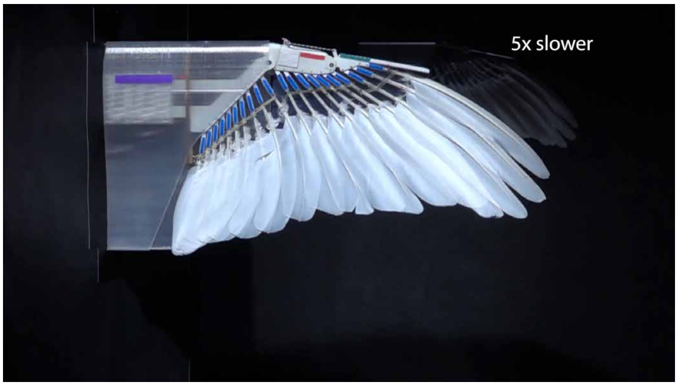

Movie 2. Morphing wing response to flexion and extension step commands of wrist and finger angle under aerodynamic loading. The wing and feather kinematics during wing flexion behave like an underdamped system, whereas during wing extension, they behave like an overdamped system.

Movie 3. PigeonBot untethered flight responses to wing asymmetry. With PigeonBot flying straight and level, we commanded wing asymmetries while locking the rudder neutral and measured the resulting kinematics. Feathered wing asymmetry causes primarily roll with adverse yaw.

Underactuated planform control

To determine how well underactuated robotic feather coordination works, we tracked the angle of all 20 feathers in one wing half and mapped its dependency on wrist and finger angle in our wind tunnel (*25*). The feather dynamics analyses show that the feathers follow the wrist and finger angle input in a quasi-static fashion, because the transfer function is dominated by the stiffness of the biomimetic elastic ligament. The aerodynamic test conditions corresponded to the mean flight speed (11.7 m/s) and angle of attack (4.4°) at which PigeonBot flies. We swept the wing through all combinations of θ_{wrist} and θ_{finger} quasi-statically at 0.4 Hz (Materials and Methods). The transfer function of each feather fits a 3D plane in the 3D parametric space of wrist-finger-feather angle (Fig. 4A). The best-fit 3D planes are described by the following linear function

$$\theta_{\text{feather}} = A^*\theta_{\text{wrist}} + B^*\theta_{\text{finger}} + \theta_{\text{offset}} \quad (5)$$

in which A is the sensitivity of feather angle (θ_{feather}) to wrist angle (θ_{wrist}), B is the sensitivity of feather angle to finger angle (θ_{finger}), and θ_{offset} is the constant offset angle of each fitted plane. The three transfer function coefficients have relatively simple trends across the secondary (S10 to S1) and primary (P1 to P10) feathers in the wing (Fig. 4B) and fit the measured data well with an average root mean square error (RMSE) of 0.87°. As in the cadaver wings, feather sensitivity to wrist and finger angle is highest for the primary feathers in the biohybrid wing. The offset angle is highest for the secondary feathers. These transfer functions between the wrist and finger angle, which are under closed-loop control via two servos, and the 20 underactuated feathers, are embodied by the elastic ligament, which determine the planform parameters of the morphing wing (Fig. 4C). Together, the wrist and finger angle control wing area, span, and aspect ratio fluidly (Fig. 4, A to C), similar to what we found for pigeon wings (Fig. 1). Consequently, the biohybrid wing offers an unusually rich set of wing planforms that can be selected for the task at hand based on just two control inputs per wing half. To determine the dynamic response of the underactuated biohybrid morphing wing, we actuated it at a range of frequencies ranging from quasi-static (0.4 Hz) to dynamic (9 Hz) over more than a 10-fold range: The system bandwidth ranges up to ~5 Hz, after which it rolls off due to servo limitations (Fig. 4D and Movie 1; see Materials and Methods for details on how we coupled the wrist and finger in this test). The somewhat reduced area under aerodynamic loading is due to wing drag, which causes the wing to not fully unfold, because the tiny servomotors in the wing are torque limited. The dynamic response rolls off around ~5 Hz, which matches the pigeon wingbeat frequency during cruising flight (*26*). With stronger servos, the biohybrid wing may thus encompass the in vivo wingbeat range up to ~7 Hz for takeoff and landing. Because birds can morph their wings into different planforms for upstrokes and downstrokes (*27*), our biohybrid wing could eventually be used to study the role of wing morphing in flapping flight. During wing extension, the dynamic response of feather angles due to step inputs of wrist and finger angle is characteristic for overdamped motion, whereas during wing flexion, the dynamic response is characteristic of underdamped motion (Fig. 4E). The analyses thus show how the underactuation mechanism of the biohybrid morphing wing functions dynamically under aerodynamic loading up to wingbeat frequencies observed in pigeons.

To characterize the dynamic response of the feathers to step input commands of the wrist and finger, we compared the feather kinematics predicted by the quasi-static feather transfer function (Eq. 5) with our dynamic morphing wing measurements (Fig. 5, A to C). We found that the feathers effectively respond quasi-statically to dynamic wrist and finger input (Fig. 5E), showing that the underactuated feather motion is dominated by the spring stiffness of the tuned rubber bands undergoing quasi-linear deformations. The associated mean RMSE feather angle error across the secondary and primary feathers for n = 10 flexion and extension cycles under aerodynamic loading (Movie 2) is only 1.31°, which is low compared with the ~70° input motion via P10 (Fig. 5D). This shows that damping and inertia effects are minimal. The corresponding small standard deviations confirm that the underactuated feather motion is highly repeatable (Fig. 5D). Consequently, the difference in the observed feather extension versus flexion kinematics (Fig. 5C) is primarily driven by the difference in the wrist and finger extension versus flexion dynamics (Fig. 5, A and B). The domination of static over dynamic effects in the feather transfer functions is confirmed by an order-of-magnitude analysis for the fundamental natural frequency, f_0, of the elastic ligament, with stiffness, $k \approx 100$ N/m, that connects the feathers with mass, $m \approx 0.0001$ kg, using Rayleigh's method based on estimating the ratio of potential and kinetic energy of the ligament undergoing harmonic motion

$$O[f_0] = O\left[\frac{1}{2\pi}\sqrt{\frac{X^T K X}{X^T M X}}\right] = O\left[\text{const}\cdot\frac{1}{2\pi}\sqrt{\frac{L^2 k}{R^2 m}}\right] = \frac{1}{2\pi}\frac{L}{R}\sqrt{\frac{k}{m}} = 50\ \text{Hz} \tag{6}$$

where X is the assumed displacement vector; K and M are the generalized stiffness and mass matrices, respectively; $L \approx 0.02$ m is the distance of the spring attachment with respect to the pin joint; and $R \approx 0.06$ m is the estimated distance from the pin joint to the center of mass of the feather (see the Supplementary Materials for details), and we assumed that the constant is reasonably close to 1 (*28*). The fundamental natural frequency of the ligament (~50 Hz; Eq. 6) versus the maximal servo actuation frequency before roll-off (~5 Hz; Fig. 4D), $f_0/f_s \approx 10$, is thus roughly one order of magnitude higher. This shows how the bandwidth of our biohybrid morphing wing (Fig. 4D) is limited by the servo actuators, because the elastic ligament's dynamic response is stiffness dominated and thus quasi-static (*28*). This further explains why the flexible flight feathers never flutter despite their elastic connectivity and dynamic actuation under aerodynamic loading (Fig. 5 and Movies 1 to 3). The stiffness-dominated transfer functions observed in our roboticized biohybrid wing (Figs. 4 and 5) are thus analogous to the linear elastic transfer functions that we observed in the animated pigeon wings (Fig. 1D). That is, in contrast to aircraft wings, which are either designed to be stiff or outfitted with an active aeroelastic response suppression system (*29*), we observe that bird flight feathers form a flexible and soft wing that can dynamically morph with stable aeroelastic transfer functions (Fig. 5, A to C, and Movies 1 to 3). We further tested the robustness of this finding by morphing the wings in high turbulence and found similarly stable feather transfer functions and accompanying stable aeroelastic responses, aided by a micromechanical locking mechanism between the feathers that prevents gaps from forming in the wing planform, which we report in detail elsewhere (*30*).

Asymmetric aerodynamic coupling

To understand how asymmetric wing morphing may initiate turn maneuvers, we developed an aerodynamic model based on the Athena vortex lattice (AVL) method (*31*), which shows that asymmetric wing morphing causes adverse roll-yaw coupling due to induced drag asymmetry (Fig. 6). AVL is a vortex lattice code that simulates the lifting line using horseshoe vortex elements for simulating the potential flow around the wing, which gives estimates of both lift and induced drag but ignores viscous effects such as the boundary layer. The computational efficiency of this code allowed us to test a large number of cases, whereas more complex codes are too computationally expensive to make our comparisons (*32*). Earlier estimates of potential versus viscous flow effects show that the wing profile drag is slightly higher than the induced drag for our flight conditions in pigeons, up to about twice as high (*21*). It is thus fair to assume that although our simulations underestimate adverse yaw affects somewhat, they are sufficiently accurate to gain useful insight into adverse yaw affects due to wing morphing.

By simulating 169 simplified PigeonBot wing planforms (Fig. 6A) during straight flight at pigeon glide speeds (*18*) under 1*g* wing loading (for details, see Materials and Methods), we found that asymmetric planform morphing causes the swept back wing to roll down to initiate a turn as desired (Fig. 6C), while yaw moments act in the opposite direction of turning (Fig. 6D). The simulations thus predict adverse yaw due to asymmetric wing morphing. However, the rolling moment dominates the adverse yaw moment by a factor of ~10, with the yaw-to-roll ratio maximum occurring at slightly asymmetric tucked planforms (Fig. 2E). On the basis of these results, we hypothesize that birds use their tails to generate lateral forces (*33*) to counteract adverse yaw due to asymmetric wing morphing.

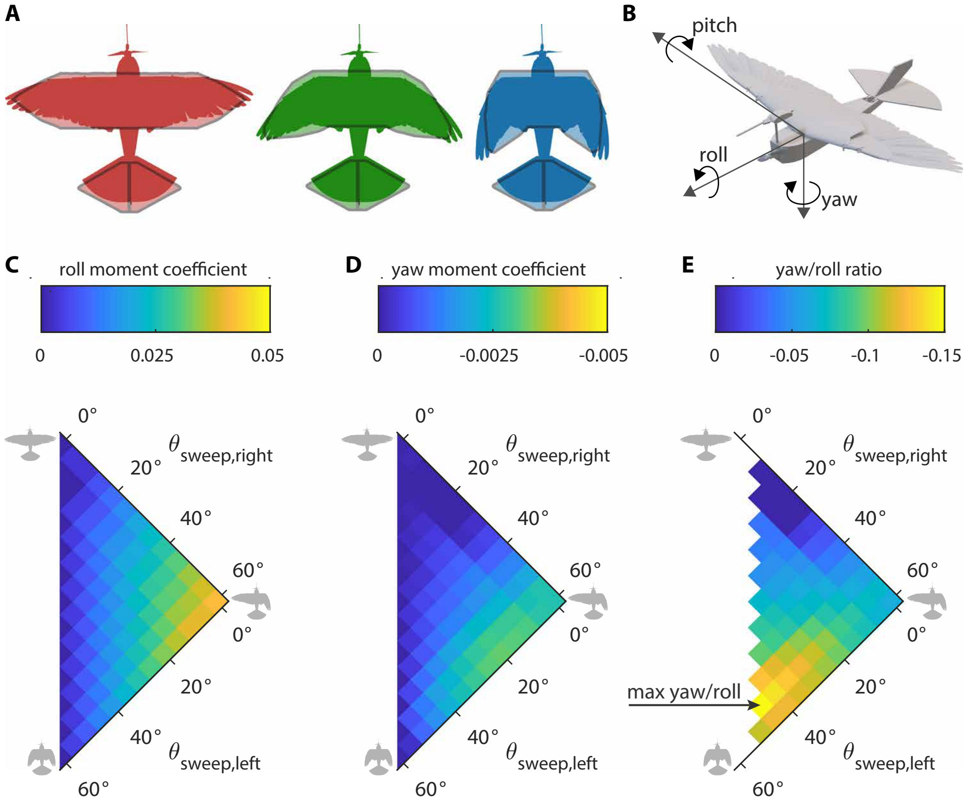

Fig. 6. Aerodynamic simulations predict coupled roll and adverse yaw due to asymmetric morphing. (**A**) We approximate PigeonBot's geometry using quantized wing geometries for aerodynamic simulations with the potential flow code AVL (*31*). (**B**) Moment coefficient results are reported in the reference frame shown, with positive roll and yaw indicating a right-hand turn. Simulating combinations of left ($\theta_{\text{sweep, left}}$) and right ($\theta_{\text{sweep, left}}$) wing morphing in steps of 5° shows coupled roll (**C**) and yaw (**D**) moment coefficients generated by the resulting 169 wing planforms. Positive roll moment coefficients with negative yaw moment coefficients indicate adverse yaw. (**E**) Ratio of yaw-to-roll moment coefficients shows peak adverse yaw ratios for slightly asymmetric tucked wings. The robot can minimize adverse yaw by harnessing extended wings that are only slightly asymmetric, combining symmetric extended wrist angles with asymmetric finger angles (symmetric wing configurations are not shown to avoid dividing by zero).

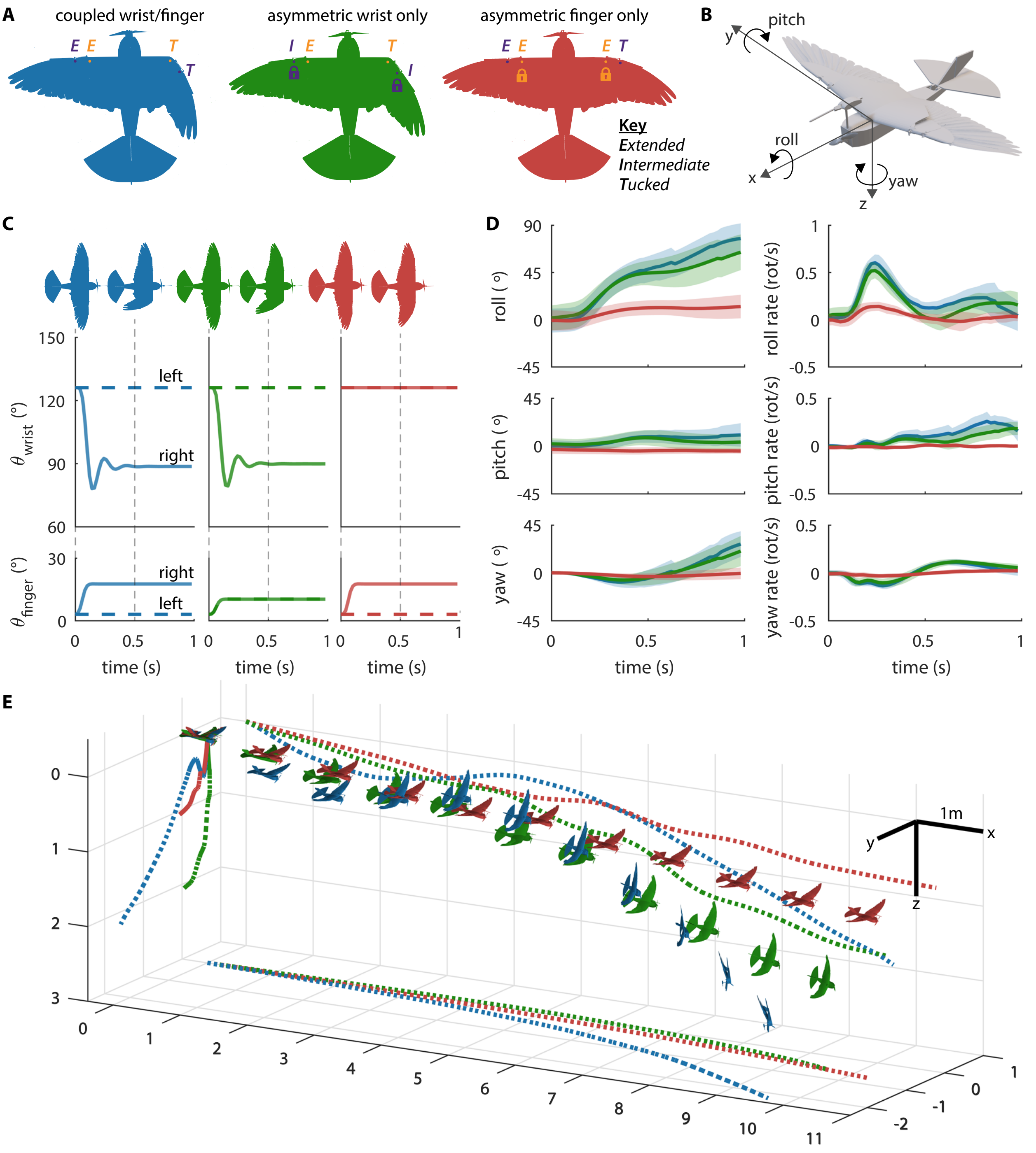

Fig. 7. Asymmetric morphing wing flight tests reveal initial coupled roll and adverse yaw dynamics. (**A**) We tested open-loop dynamics due to asymmetric wing morphing using three experimental permutations: coupled wrist/finger asymmetry (blue) with left finger and wrist extended, right wrist and finger tucked; wrist asymmetry only (green) with both fingers intermediate, left wrist extended, right wrist tucked; and finger asymmetry only (red) with both wrists extended, left finger extended, right finger tucked. Lock icons indicate that left and right joints are the same angle. (**B**) The measurement results are reported in the reference frame shown, with positive roll and yaw indicating a right-hand turn. (**C**) Using our wing kinematics model (Eq. 7 based on Fig. 5, A and B), we estimated the time-resolved wing position for the step response commands for the three wing asymmetry cases shown in (A). Solid lines indicate the average and shaded regions indicate the standard deviation. (**D**) Roll, pitch, and yaw responses of the robot to the three wing asymmetry cases in (A) reveal a dominant roll response coupled with adverse yaw initially for the wrist asymmetry cases. The finger asymmetry case has no appreciable adverse yaw. Once the robot has rolled sufficiently into the turn, the adverse yaw angle changes direction, yawing into the turn instead ($n = 12$; 6 right + 6 left asymmetry trials pooled). Rotation rates are reported in full rotations per second. (**E**) A 3D reconstruction of a representative trial from each wing asymmetry variation in (A); the 3D flight paths are plotted in 0.1-s increments and projected on the (x,y), (x,z), and (y,z) plane for comparison.

Wrist- and finger-controlled turn initiation

On the basis of pilot tests with our intermediate morphing wing prototypes (Fig. 2E), we confirmed earlier reports that asymmetric wing tips make aerial robots roll (*20*). In addition to a biomimetic wrist, our biohybrid robot features a finger joint, which raises the question how each contributes to turning flight control, considering that we demonstrated that they both modify the wing planform (Fig. 4). Our flight results show that PigeonBot can initiate turns through both wrist- and finger-based asymmetric wing morphing, with the wrist giving coarse control and the finger fine control (Fig. 7 and Movie 3). We established this based on the following flight test matrix: 3 wrist-finger coupling variations (coupled, wrist only, and finger only) × 3 wing asymmetry variations (extended and intermediate, intermediate and tucked, and extended and tucked) × 2 wing sides (left and right) × 6 trials each (alternating heading approximately north and south) = 108 flights total. After determining that left versus right wing morphing gave sufficiently similar results, we pooled the data (Figs. 7 and 8). We characterized the open-loop dynamic response due to wing morphing by commanding step inputs to θ_{wrist} and θ_{finger} while the rudder was locked to a neutral position. During these automated trials, the PixRacer controlled the elevator under closed-loop control to sustain the robot's pitch (details in Materials and Methods).

Coupled wrist and finger asymmetry initiates roll over large angles and results in strong flight-path curvature, whereas fine finger asymmetry in extended wings initiates roll over small angles, which saturates at semiconstant roll angles and modest flight path curvatures. To estimate the dynamic wrist and finger angle changes in flight (Fig. 7C) as a function of step inputs, we fit the wrist and finger angles from wind tunnel data under approximate flight conditions (Fig. 5, A and B) to a simple mass-spring-damper system

$$\theta_{\text{actuator}}(t) = \frac{1}{k}u(t) - \frac{m}{k}\ddot{\theta}_{\text{actuator}}(t) - \frac{c}{k}\dot{\theta}_{\text{actuator}}(t) + \theta_0 \qquad (7)$$

where k is the spring coefficient; c is the damper coefficient; m is the mass coefficient; $u(t)$ is the nominal commanded step input; and $\theta_{\text{actuator}}, \dot{\theta}_{\text{actuator}}$, and $\ddot{\theta}_{\text{actuator}}$ are wrist or finger angles, angular velocities, and angular accelerations, respectively (RMSE: 4.0° for θ_{wrist} and 2.2° for θ_{finger}). The measured roll, pitch, and yaw responses in flight show that, in contrast to aileron-initiated roll in aircraft, which asymptotes to a constant roll rate (*34*), PigeonBot's roll rate first steeply increases, after which it peaks and then decreases again to lower values close to zero (Fig. 7D). Although the turn experiments did not last long enough to fully establish roll angle saturation for the wrist asymmetry cases, the finger-induced roll angle saturates. This suggests that finger angle controls roll angle instead of roll rate (Fig. 7C). The wrist data similarly suggest that asymmetric wing morphing ultimately controls roll angle, because roll angle does plateau over the time course of the flight tests for less aggressive wrist asymmetries (Fig. 8, C and F). Furthermore, whereas large wing asymmetries cause adverse yaw responses initially as predicted by our model (Fig. 6), they quickly resolve, and PigeonBot continues to yaw into the turn as desired (Fig. 7D). Such initial adverse yaw effects could not be distinguished for finger-based control, which agrees with our aerodynamic roll/yaw coupling model for fully extended wings. Last, we compare both roll angle and turn curvature for different combinations of wrist angles to evaluate wrist- and finger-dominated turn initiation (Fig. 8). Our data show that large-amplitude wrist-based control is not distinguishably modulated by finger motion (green and blue traces in Fig. 8) and that finger-based control is effective in fully extended wings (red traces in Fig. 8, B, C, H, and I).

DISCUSSION

Inspired by how gliding pigeons morph their wing planform in flight, we developed a novel biohybrid morphing wing with 40 underactuated flight feathers controlled by two wrists and two fingers under closed-loop control. On the basis of pigeon cadaver studies, we corroborated that both the wrist and finger drive feather angle in an approximately linear fashion. Using our biohybrid wind tunnel model, we determined that this provides effective control over wing span, area, and aspect ratio in the left and right wing under aerodynamic loading. By analyzing the associated feather kinematics during rapid morphing, we found that the underactuated feathers respond quasi-statically to wrist and finger input, guided by the biomimetic elastic ligament. The measured aeroelastic responses of the soft feathered wing are stable and thus flightworthy. We then tested how effective asymmetric morphing initiates turning flight with our PigeonBot. The data show that wrist-based planform asymmetry offers coarse control and finger-based asymmetry in fully extended wings offers fine control. Wrist-based morphing was previously demonstrated in aerial robots with morphing hand wings consisting of stiff artificial feathers in symmetric (*18*) and asymmetric (*20*) flight. Here, we extend this work to soft biohybrid morphing wings in which both the arm and hand wing consists of real pigeon flight feathers. Another advance is that the pigeon feathers are underactuated through tuned elastic coupling. Our biohybrid pigeon wing forms the most comprehensive flying model of a morphing bird wing to date, harnessing real flight feathers that are incredibly soft, light, and robust and feature stable aeroelastic responses under variable aerodynamic loading. Hence, PigeonBot offers a first step toward the replacement (*35*) of some invasive bird research experiments—offering more humane and improved control over wing shape than possible in vivo.

The underactuated morphing wing principles presented here may inspire more economical and simpler morphing wing designs for aircraft and robots with more degrees of freedom than previously considered. Our results show how a properly designed underactuated morphing wing requires markedly fewer sensors and actuators, creating a lighter, more economical, and more reliable aerial robot that can harness many more separate morphing elements in flight than previously reported in the literature (*18*–*20*). The mechanism design and kinematic performance of our biohybrid robotic wing show how wrist and finger angle can markedly change wing shape parameters while offering the opportunity to keep one planform parameter constant and simultaneously varying another. During flight testing, we found that the adverse yaw effects predicted by our computational model are initially present for large wrist asymmetries before the desired yaw response commences. This suggests a role for a biohybrid morphing tail to combat adverse yaw and minimize slip (*36*). Finger asymmetry, on the other hand, does not induce noticeable adverse yaw.

PigeonBot shows that birds may steer their gliding flight with their fingers, although in vivo research is needed to confirm this. Our data further suggest that birds use asymmetric wing morphing to control roll position instead of roll rate, possibly going from one stable roll attractor in parametric space to another. We hypothesize

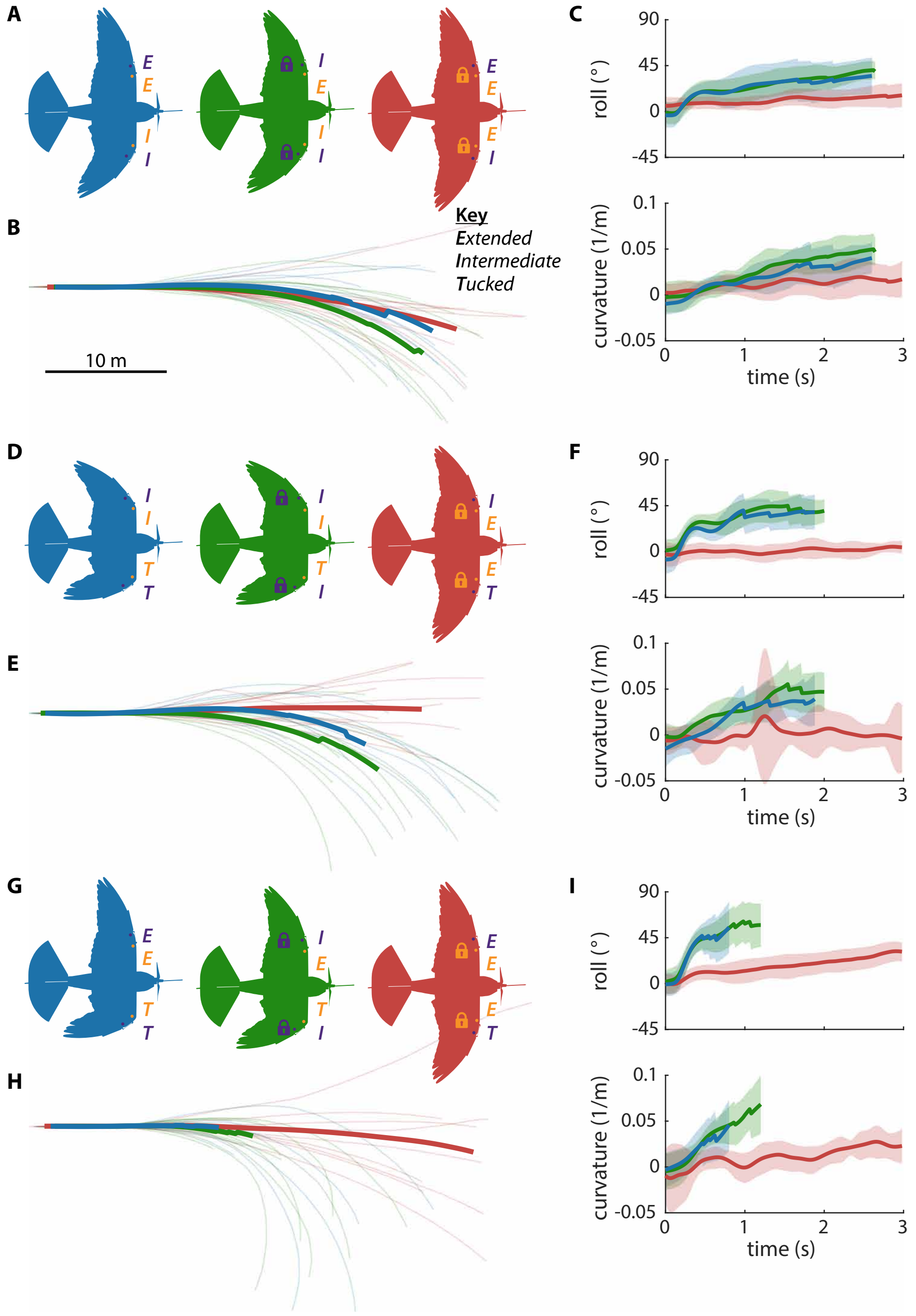

Fig. 8. Asymmetric morphing wing flight tests reveal that finger motion alone can control steady-state turns. We measured open-loop dynamics of nine permutations of wing asymmetry cases, including extended/intermediate variations (**A**), intermediate/tucked variations (**D**), and extended/tucked variations (**G**) (Fig. 7) with coupled wrist/finger (blue), wrist asymmetry only (green), and finger asymmetry only (red) (**B**, **E**, and **H**). Projected top-down flight traces show that PigeonBot can control turns based on minor finger flexion asymmetry alone [red traces in (G), (H), and (I)]. (**C**, **F**, and **I**) Once past the initial response, most responses to wing asymmetry result in an equilibrium roll angle and turn curvature. Solid lines indicate the average and shaded regions indicate the standard deviation.

that control of roll angle instead of roll rate may simplify flight in unsteady wind environments; testing this idea requires further study with better flying biohybrid models. Future biohybrid bird studies based on cadavers of naturally deceased birds could sample among 10,000 extant bird species—offering unprecedented comparative research opportunities without ecological or welfare impact. More sophisticated models could harness improved servo actuators, adding covert and other feathers for further streamlining, or apply taxidermy techniques and more actuated degrees of freedom to make the biohybrid bird extremely lifelike. The wings could integrate additional degrees of freedom, such as wing twist (*3*), or add an alula (*37*), whereas the conventional tail could be replaced with a biohybrid morphing tail to make the robot much more maneuverable (*36*). Integrating more sensors, such as machine vision for autonomous flight (*38*), could test advanced bird flight control hypotheses (*39*). These sophisticated "animatronic models" could also integrate flapping wings (*40*) for propulsion. The morphing wings could also be designed so that they fully fold away during diving (*41*) and allow for swimming in water (*42*) and locomotion on land (*43*). Applications include entertainment and nonintrusive environmental and ecological surveys, as well as deterring bird pests. Our main purpose for creating biohybrid robots is, however, developing a better scientific model to advance our understanding of how birds outfly robots.

MATERIALS AND METHODS

Pigeon wing measurements and feathers

We used motion capture cameras to track the 3D coordinates of 20 remiges as well as the four major wing bones (Fig. 1). To track the bones, we inserted marker clusters with retroreflective markers in the left wing of pigeon cadavers (*C. livia*, $N = 3$). To track the feathers, we adhered two markers with 2.4-mm diameters at least 10 mm apart on the ventral side of each rachis for all remiges with cyanoacrylate. The fabrication and insertion and imaging of triangular marker clusters in the major wing bones of the pigeon cadaver have been described in detail by Stowers *et al.* (*14*). Six motion capture cameras [Qualisys Oqus 7+; 12 megapixels (MP), 300 Hz] were used to track markers; a seventh recorded video at 30 Hz. Tracking residual was below 0.1 mm; for more details, see Stowers *et al.* (*14*). To reduce noise, we filtered the tracked marker position data with a fourth-order low-pass Butterworth filter with a cutoff frequency of 8 Hz. Therefore, although feather angles did vary continuously for each trial, the plots feature jitter introduced by marker occlusion as well as data points from some trials that were binned into some bins but not others. Most of the jitter fell, however, outside of PigeonBot's morphing range (Fig. 1D; see Supplementary Text for details). All experimental procedures were conducted on pigeon cadavers and approved by Stanford's Administrative Panel on Laboratory Animal Care.

To perform the principal components analysis on the wing bone kinematics, we created computational markers that defined a wing axis for each wing bone (see Supplementary Text for details). We then placed the x, y, and z positions of our $n = 16$ points (four on each bone) over $N = 500$ time steps into an $N \times 3n = 500 \times 48$ matrix, A, to compute the correlation matrix, R, as

$$R = \frac{1}{N} A^T A \tag{8}$$

in which the principal components are equal to the eigenvectors of R with corresponding eigenvalues, λ_i. The eigenvectors represent the amount of motion of each principal component. In particular, component i makes up

$$\frac{\lambda_i}{\sum_{k=1}^{3n} \lambda_k} \% \tag{9}$$

of the measured motion.

Biohybrid wing design

The wing skeletal structure was 3D printed in nylon, and the fixed wing root airfoil was formed by balsa ribs with a Wortmann FX 60-126 airfoil covered by cardstock. To actuate the 3D printed skeletal structure, we used Turnigy T541BBD servos for the wrist joints and HK-282A servos for the finger joints in the final biohybrid wing design (Fig. 2E). To minimize friction, we inserted a Teflon sheet between sliding surfaces of the pin joints of the feather interfaces. We developed a biomimetic wing root airfoil by fitting published 3D in vivo pigeon wing airfoil data, measured during gliding (*23*), to an existing database of more than 1500 low–Reynolds number airfoils (https://m-selig.ae.illinois.edu). We normalized all airfoils to the same size and incidence angle and independently calculated the RMSE of every airfoil comparison's top and bottom surface. The best-fit (most biomimetic) airfoil was the Wortmann FX 60-126 (RMSE: 0.99% chord length). The total weight of PigeonBot is 280 g, whereas pigeons are comparatively heavier at ~400 g (*18*).

Biohybrid wing wind tunnel experiments

We filmed the kinematics of the biohybrid wing in a wind tunnel (*25*) and used colored markers applied to the 3D printed skeletal structure and each feather to track their position over time. A left wing was mounted on a splitter plate, with the wind speed and the angle of attack set to 11.7 m/s and 4.4°, respectively, matching the outdoor flight conditions measured during symmetric flight trials. The axial wind tunnel turbulence intensity was 2.7% (Campbell CSAT3B anemometer). We controlled the wing servos with a servo controller (Pololu Micro Maestro) running custom scripts. All angles and wing shapes were automatically image-tracked with a custom MATLAB script (MATLAB R2017b).

During quasi-static experiments (Fig. 4, A to C), we commanded the biohybrid wing to slowly sweep through its full range of motion for combinations of θ_{wrist} and θ_{finger} by continually cycling θ_{wrist} at 0.4 Hz while cycling θ_{finger} at 0.01 Hz. We recorded video of the wing at 50 Hz (Nikon D500, 2.1 MP with Nikon 18-135 mm f/3.5-5.6G ED-IF AF-S DX lens). We fitted the data to a linear model using MATLAB's fit function.

For the dynamic response experiments, we conducted bandwidth and step response tests. For the bandwidth tests, we commanded the actuators to flex ($\theta_{\text{wrist}} = 85°$, $\theta_{\text{finger}} = 16°$) and extend ($\theta_{\text{wrist}} = 135°$, $\theta_{\text{finger}} = -4°$) 20 cycles with linear servo motion at increasingly high frequency from 0.4 to 8.9 Hz. We recorded video for these tests at 100 Hz (Sony DSC-RX10 III, 2.1 MP). For the step response tests, we commanded the servo actuators to flex ($\theta_{\text{wrist}} = 85°$, $\theta_{\text{finger}} = 16°$) and extend ($\theta_{\text{wrist}} = 135°$, $\theta_{\text{finger}} = -4°$) for 10 cycles at their maximum speed. We recorded video for these tests at high speed, 250 Hz (Sony DSC-RX10 III, 2.1 MP). We calculated angular velocities and angular accelerations from recorded angles using a central difference scheme. We fitted the mass-spring-damper models to the measured wrist and finger angle kinematics using MATLAB's fitnlm function.

Aerodynamic simulations

We performed aerodynamic simulations of morphed wing planforms using AVL 3.35 (*31*). We approximated PigeonBot's wing geometry and mass properties by generating quantized planforms with a custom MATLAB script for sweep angles ranging from 0° to 60° at increments of 5° for each wing for a total of 169 wing sweep pairs. All 169 wing sweep pairs were simulated with the same static horizontal and vertical tail at 0° incidence angle. We constrained the calculations for angles of attack for which the lift force predicted by AVL balanced the weight of PigeonBot (1*g* loading for a mass of 255 g, earlier version of PigeonBot) at an airspeed representative for the planform wing area. We calculated this representative airspeed as a function of planform area by linearly interpolating pigeon glide speed as a function of the measured wing area in vivo (*18*).

Biohybrid robot outdoor free-flight experiments

The PigeonBot control and data logging system consists of an electric propulsion system, elevator, rudder, autopilot, radio transceivers, and a battery (see table S4 and the Supplementary Materials for details). All sensors except for GPS sampled at 50 Hz. The GPS sampled at 5 Hz. We defined the 3D orientation of the robot as a series of three sequential body-fixed yaw, pitch, then roll Euler angles, calculated from the autopilot's estimate of vehicle orientation based on its extended Kalman filter. For roll, pitch, and yaw rates, we used the direct gyroscope measurement. We used GPS coordinates converted to a cardinal reference frame at the measured GPS x,y flight location combined with the z altitude from the barometer to reconstruct the robot's x,y,z position with respect to the ground.

To test the robot's open-loop response to wing morphing asymmetry, we used a sequence of flight modes that transferred the robot from manual teleoperation to autopilot-assisted steady level flight and then to an automated wing asymmetry trial (details in the Supplementary Materials). The automated flight trial mode commanded a predetermined asymmetric wing planform while simultaneously locking the rudder in its neutral position and the throttle at 68%. The elevator was under autopilot control during the trial to maintain a level pitch orientation [ArduPilot v3.8.3 FLY BY WIRE_A (FBWA)]. We only analyzed and plotted flight data recorded during automated asymmetric wing morphing flight trials in which all actuators were locked except for the elevator under autopilot control. The pilot had no influence on the recorded data reported; his only function was to take control after the automated trial.

To align each projected *x*,*y*,*z* flight trace in Fig. 8, we calculated the ground heading of each trial by comparing GPS coordinates at the moment we engaged wing asymmetry and 0.5 s before that time. We then rotated each north/south trial as shown in the figures so that each trial began flying left to right with the same heading. We excluded four trials with GPS tracking errors due to a recorded horizontal dilution of precision greater than 1.8, totaling 3.7% of the total number of trials. To calculate the averaged traces shown in Fig. 8, we calculated the mean position from all valid trials at each time step until only 75% of trials remained, resulting in averaging over a minimum of nine trials for each averaged trace.

SUPPLEMENTARY MATERIALS

robotics.sciencemag.org/cgi/content/full/5/38/eaay1246/DC1
Supplementary Text
Fig. S1. Rubber band force versus length properties.
Fig. S2. Templates used for rubber band selection and tuning.
Table S1. PigeonBot feathers were 90% from the same individual; the wind tunnel model feathers were 100% from the same individual.
Table S2. Rubber bands used to connect PigeonBot feathers.
Table S3. Rubber bands used to connect wind tunnel model feathers.
Table S4. Bill of materials for constructing PigeonBot.
References (*45*, *46*)

REFERENCES AND NOTES

1. E. Torenbeek, *Synthesis of Subsonic Airplane Design* (Delft Springer, 1982).
2. M. H. Sadraey, *Aircraft Design: A Systems Engineering Approach* (John Wiley & Sons, 2012).
3. G. K. Taylor, A. C. Carruthers, T. Y. Hubel, S. M. Walker, *Morphing Aerospace Vehicles and Structures* (John Wiley & Sons Ltd., 2012), pp. 11–40.
4. D. D. Chin, L. Y. Matloff, A. K. Stowers, E. R. Tucci, D. Lentink, Inspiration for wing design: How forelimb specialization enables active flight in modern vertebrates. *J. R. Soc. Interface* **14**, 20170240 (2017).
5. D. Lentink, U. K. Müller, E. J. Stamhuis, R. de Kat, W. van Gestel, L. L. Veldhuis, P. Henningsson, A. Hedenström, J. J. Videler, J. L. van Leeuwen, How swifts control their glide performance with morphing wings. *Nature* **446**, 1082–1085 (2007).
6. A. Hedenström, G. Norevik, K. Warfvinge, A. Andersson, J. Bäckman, S. Åkesson, Annual 10-month aerial life phase in the common swift Apus apus. *Curr. Biol.* **26**, 3066–3070 (2016).
7. S. Barbarino, O. Bilgen, R. M. Ajaj, M. I. Friswell, D. J. Inman, A review of morphing aircraft. *J. Intell. Mater. Syst. Struct.* **22**, 823–877 (2011).
8. E. Nissim, Effect of control surface mass unbalance on the stability of a closed-loop active control system, in *30th Structures, Structural Dynamics and Materials Conference* (American Institute of Aeronautics and Astronautics, 1989), pp. 476–486.
9. B. Siciliano, O. Khatib, *Springer Handbook of Robotics* (Springer, 2008).
10. J. W. Bahlman, S. M. Swartz, K. S. Breuer, Design and characterization of a multi-articulated robotic bat wing. *Bioinspir. Biomim.* **8**, 016009 (2013).
11. J. A. Cheney, N. Konow, K. M. Middleton, K. S. Breuer, T. J. Roberts, E. L. Giblin, S. M. Swartz, Membrane muscle function in the compliant wings of bats. *Bioinspir. Biomim.* **9**, 025007 (2014).
12. A. Ramezani, S.-J. Chung, S. Hutchinson, A biomimetic robotic platform to study flight specializations of bats. *Sci. Robot.* **2**, eaal2505 (2017).
13. C. J. Pennycuick, *Modelling the Flying Bird* (Elsevier Science, 2008).
14. A. K. Stowers, L. Y. Matloff, D. Lentink, How pigeons couple three-dimensional elbow and wrist motion to morph their wings. *J. R. Soc. Interface* **14**, 20170224 (2017).
15. A. M. Lucas, P. R. Stettenheim, *Avian Anatomy: Integument* (U.S. Department of Agriculture, 1972).
16. T. L. Hieronymus, Flight feather attachment in rock pigeons (Columba livia): Covert feathers and smooth muscle coordinate a morphing wing. *J. Anat.* **229**, 631–656 (2016).
17. J. C. Rüegg, Smooth muscle tone. *Physiol. Rev.* **51**, 201–248 (1971).
18. D. Lentink, "Exploring the biofluiddynamics of swimming and flight," thesis, Wageningen Univerity, Wageningen, the Netherlands (2008).
19. M. A. Snook, Variable geometry wing, WO2014041198A1 (2014).
20. M. Di Luca, S. Mintchev, G. Heitz, F. Noca, D. Floreano, Bioinspired morphing wings for extended flight envelope and roll control of small drones. *Interface Focus* **7**, 20160092 (2017).
21. C. J. Pennycuick, A wind-tunnel study of gliding flight in the pigeon Columba Livia. *J. Exp. Biol.* **49**, 509–526 (1968).
22. J. J. Videler, *Avian Flight* (Oxford Univ. Press, 2006).
23. W. Biesel, H. Butz, W. Nachtigall, Erste Messungen der Flügelgeometrie bei frei gleitfliegenden Haustauben (*columbia livia var. domestica*) unter Benutzung neu ausgearbeiteter Verfahren der Windkanaltechnik und der Stereophotogrammetrie. *Biona-Rep.* **3**, 139–160 (1985).
24. R. Tedrake, *Underactuated Robotics: Algorithms for Walking, Running, Swimming, Flying, and Manipulation (Course Notes for MIT 6.832)*. Downloaded on 11/29/2019 from http://underactuated.mit.edu/.
25. D. B. Quinn, A. Watts, T. Nagle, D. Lentink, A new low-turbulence wind tunnel for animal and small vehicle flight experiments. *R. Soc. Open Sci.* **4**, 160960 (2017).
26. C. J. Pennycuick, Power requirements for horizontal flight in the pigeon Columba livia. *J. Exp. Biol.* **49**, 527–555 (1968).
27. A. M. Berg, A. A. Biewener, Kinematics and power requirements of ascending and descending flight in the pigeon (Columba livia). *J. Exp. Biol.* **211**, 1120–1130 (2008).
28. W. Thomson, *Theory of Vibration with Applications* (CRC Press, 2018).
29. P. P. Friedmann, Renaissance of aeroelasticity and its future. *J. Aircr.* **36**, 105–121 (1999).
30. L. Y. Matloff, E. Chang, T. J. Feo, L. Jeffries, A. K. Stowers, C. Thomson, D. Lentink, How flight feathers stick together to form a continuous morphing wing. *Science* **367**, 293–297 (2020).
31. M. Drela, H. Youngren, AVL (Athena Vortex Lattice) (2007); http://web.mit.edu/drela/Public/web/avl/.
32. J. Larsson, Q. Wang, The prospect of using large eddy and detached eddy simulations in engineering design, and the research required to get there. *Philos. Trans. A Math. Phys. Eng. Sci.* **372**, 20130329 (2014).
33. R. G. Hoey, Exploring bird aerodynamics using radio-controlled models. *Bioinspir. Biomim.* **5**, 045008 (2010).
34. R. C. Nelson, *Flight Stability and Automatic Control* (WCB/McGraw Hill, 1998), vol. 2.
35. W. M. S. Russell, R. L. Burch, C. W. Hume, *The Principles of Humane Experimental Technique* (Methuen, 1959), vol. 238.
36. J. A. Gillies, A. L. R. Thomas, G. K. Taylor, Soaring and manoeuvring flight of a steppe eagle Aquila nipalensis. *J. Avian Biol.* **42**, 377–386 (2011).
37. B. A. Mandadzhiev, M. K. Lynch, L. P. Chamorro, A. A. Wissa, An experimental study of an airfoil with a bio-inspired leading edge device at high angles of attack. *Smart Mater. Struct.* **26**, 094008 (2017).
38. R. Kennedy, P. Henry, H. Maritrosyan, J. Zhu, A. Bachrach, A. Bry, Image space motion planning of an autonomous vehicle, U.S. Patent US20190050000A1 (2019).
39. D. L. Altshuler, M. V. Srinivasan, Comparison of visually guided flight in insects and birds. *Front. Neurosci.* **12**, 157 (2018).
40. G. A. Folkertsma, W. Straatman, N. Nijenhuis, C. H. Venner, S. Stramigioli, Robird: A robotic bird of prey. *IEEE Robot. Autom. Mag.* **24**, 22–29 (2017).
41. C. H. Brighton, A. L. Thomas, G. K. Taylor, Terminal attack trajectories of peregrine falcons are described by the proportional navigation guidance law of missiles. *Proc. Natl. Acad. Sci. U.S.A.* **114**, 13495–13500 (2017).
42. R. Siddall, M. Kovač, Launching the AquaMAV: Bioinspired design for aerial–aquatic robotic platforms. *Bioinspir. Biomim.* **9**, 031001 (2014).
43. W. R. Roderick, M. R. Cutkosky, D. Lentink, Touchdown to take-off: At the interface of flight and surface locomotion. *Interface Focus* **7**, 20160094 (2017).
44. N. S. Proctor, P. J. Lynch, *Manual of Ornithology: Avian Structure & Function* (Yale Univ. Press, 1993).
45. T. Matsumoto, K. Nagayama, Tensile properties of vascular smooth muscle cells: Bridging vascular and cellular biomechanics. *J. Biomech.* **45**, 745–755 (2012).
46. J.-S. Zhao, K. Zhou, Z.-J. Feng, A theory of degrees of freedom for mechanisms. *Mech. Mach. Theory* **39**, 621–643 (2004).

Acknowledgments: We thank G. W. Reich for AFOSR flight permit support. **Funding:** This work was supported by AFOSR BRI award number FA9550-16-1-0182 and AFOSR DESI award number FA9550-18-1-0525 with special thanks to B. L. Lee, F. A. Leve, and J. L. Cambier leading the program. E.C. was supported by an NSF GRFP fellowship, A.K.S. by a NDSEG fellowship, and D.L. by NSF CAREER Award 1552419. **Author contributions:** All authors contributed to the conception and design of the study and data analysis. L.Y.M. and A.K.S. performed motion capture of pigeon wings. E.C. fabricated the robot body. A.K.S., L.Y.M., and E.C. iterated and fabricated biohybrid robot wings. E.C. performed wind tunnel and flight tests and made the figures. D.L. and E.C. wrote the paper, and all authors reviewed and contributed feedback. D.L. contributed advice and supervised the work. **Competing interests:** The authors declare that they have no competing interests. **Data and materials availability:** Motion capture data used for the principal components analysis are available at http://purl.stanford.edu/tw552tz7895. CAD model is available at http://dx.doi.org/10.6084/m9.figshare.11299313. All other data needed to evaluate the conclusions in the paper are present in the paper or the Supplementary Materials.

Submitted 28 July 2019
Accepted 17 December 2019
Published 16 January 2020
10.1126/scirobotics.aay1246

Citation: E. Chang, L. Y. Matloff, A. K. Stowers, D. Lentink, Soft biohybrid morphing wings with feathers underactuated by wrist and finger motion. *Sci. Robot.* **5**, eaay1246 (2020).

Science Robotics

Soft biohybrid morphing wings with feathers underactuated by wrist and finger motion

Eric Chang, Laura Y. Matloff, Amanda K. Stowers, and David Lentink

Sci. Robot. **5** (38), eaay1246. DOI: 10.1126/scirobotics.aay1246

Science Robotics (ISSN 2470-9476) is published by the American Association for the Advancement of Science. 1200 New York Avenue NW, Washington, DC 20005. The title *Science Robotics* is a registered trademark of AAAS.